PAPER

Check for updates

Synthesis of a Zr/Sn/Al-SBA-15 catalyst for the conversion of glucose to lactic acid

Farinaa Md Jamil, [ab] Anita Ramli, *[ab] Lim Jun Wei [ab] and Noorazlenawati Borhan[c]

This work reports the synthesis and catalytic evaluation of mono- and bimetallic Zr/Sn/Al-SBA-15 catalysts for the chemo-catalytic conversion of glucose to lactic acid. SBA-15 was modified *via* alumination to enhance Brønsted acidity and subsequently impregnated with varying loadings of zirconium and tin to introduce Lewis acid sites. Comprehensive characterization using BET, XRD, and NH_3-TPD confirmed that metal loading significantly influenced the textural and acidic properties of the catalysts. Among the monometallic variants, 2% Sn/Al-SBA-15 exhibited the highest lactic acid yield (4.1%) and glucose conversion (47.5%) under the screening conditions (200 °C, 5 bar N_2, and 3 h). Bimetallic catalysts achieved higher glucose conversions (up to 72.5%) but slightly lower lactic acid yields, likely due to side reactions and catalyst deactivation. Optimization studies identified 210 °C and 50 bar N_2 as the optimal conditions, achieving a lactic acid yield of 25.2% with 99.6% glucose conversion. The results highlight the synergistic role of Lewis and Brønsted acid sites in enhancing catalytic performance and demonstrate the potential of Zr/Sn/Al-SBA-15 catalysts for sustainable lactic acid production from biomass-derived glucose.

Introduction

Renewable resources that are obtained mainly from biomass have attracted growing interest, and they are replacing traditional chemicals based on fossil raw materials as an environmentally friendly alternative.[1] In this regard, biomass has long been considered an appealing feedstock for the sustainable production of fuels and chemicals, since global biomass production capabilities are extensive.[2] However, despite its potential as a feedstock for conversion into high-value-added chemicals, there are also bottlenecks such as limited conversion efficiency and poor selectivity.

Glucose, also known as dextrose, is one of the most abundant compounds derived from biomass.[3] Glucose is also well-known as a substrate for conversion into abundant high-value commercial chemicals such as gluconic acid,[4] arabinose,[5] xylitol,[6] formic acid[7] and lactic acid.[8] Among these chemicals, lactic acid, known as 2-hydroxypropionic acid, has been deemed one of the essential hydroxycarboxylic acids, and it can be easily converted into other crucial chemicals, for example, acrylic acid, propylene glycol, 2,3-pentanedione, pyruvic acid, and acetaldehyde. In addition, lactic acid has been widely used in food pre-processing, polymers, and cosmetics.[9]

Lactic acid has wide applications in food, feed, cosmetics, and textile industries. It is used as a monomer for producing polylactic acid, a promising biodegradable polymer. It is harmless and can be categorized as generally recognized as safe (GRAS).[10] Lactic acid (2-hydroxypropanoic acid) consists of a hydroxyl group adjacent to the carboxyl group. The hydroxyl and carboxyl groups are responsible for modifying lactic acid into other value-added chemicals such as lactic amide, lactide, pyruvic acid and acrylic acid, which are useful in many applications.[3] Commercial lactic acid is obtained from two major sources, namely, catalytic and biotransformation routes. About 90% of global LA production is through lactic fermentation of lactose, corn starch, grape glucose, and sugarcane sucrose. The remaining LA is produced by the catalytic route.[10]

However, one possible route to lactic acid production has been introduced using a chemocatalytic process. This process involves using chemical catalysts to accelerate and control the chemical reaction. The catalyst can be homogeneous (dissolved in the reaction medium) or heterogeneous (solid catalysts in a different phase than the reactant). This process is considered a green and sustainable approach because it efficiently utilizes renewable biomass resources to achieve high yields under relatively mild conditions.[11] Compared to homogeneous catalysts, research has increasingly focused on heterogeneous catalysts because they are more stable under the reaction

[a]HICoE Centre of Biofuel and Biochemical Research, Universiti Teknologi PETRONAS, Seri Iskandar 32610, Perak, Malaysia. E-mail: anita_ramli@utp.edu.my; farinaa. jamill@utp.edu.my; junwei.lim@utp.edu.my

[b]Department of Applied Science, Universiti Teknologi PETRONAS, Seri Iskandar 32610, Perak, Malaysia

[c]PETRONAS Research Sdn Bhd, Block C, Lot 3288 & 3289, Off Jalan Ayer Itam, Kawasan Institusi Bangi, 43000 Bangi, Selangor, Malaysia. E-mail: noorazlenawati_borhan@petronas.com

conditions, exhibit less deactivation and metal leaching, and, most importantly, offer recyclability. These advantages make heterogeneous catalysts particularly suitable for industrial applications.

Several studies have investigated catalysts for converting glucose into lactic acid, with heterogeneous Sn-Beta zeolite catalyst recognized as among the most efficient due to its Lewis acidity and well-defined pore structure. As summarized in Table 1, supported catalysts generally achieve high glucose conversion and lactic acid yields, highlighting the importance of the catalyst surface area and the presence of both Lewis and Brønsted acid sites, which act synergistically during the reaction. This is because a high surface area can allow more Lewis and Brønsted active sites to perform effectively in the reaction. For example, Sn-Beta zeolites demonstrate glucose conversions up to 98% with lactic acid yields around 48–76% under moderate temperatures (180–200 °C) and atmospheric to moderate pressures, with good recyclability maintained after multiple cycles.[12,15,16] This enhanced catalytic performance arises from the uniform dispersion of Sn species in the beta-zeolite framework, which provides accessible Lewis acid sites essential for glucose isomerization and retro-aldol reactions leading to lactic acid formation. Additionally, catalytic stability ensures reproducibility and the potential for industrial scalability. Thus, the combination of high surface area, tailored acidity, and structural stability in supported catalysts such as Sn-Beta zeolites plays a pivotal role in efficient glucose conversion to lactic acid.

Studies on different metal oxides have been reported by W. Panya et al.[18] using various transition-metal oxides such as ZrO_2, Al_2O_3, TiO_2, Fe_3O_4, V_2O_5, CeO_2, Y_2O_3, Tm_2O_3, HfO_2, Ga_2O_3, MgO, La_2O_3, Nb_2O_5 and Ta_2O_5 on the catalytic conversion of cellulose to lactic acid. Of these catalysts, ZrO_2 exhibited the highest catalytic activity, with a lactic acid yield of 21.2% at a reaction temperature of 473 K. The lactic acid yield increased to 25.3% when ZrO_2 was impregnated on an Al_2O_3 support. In this system, the role of the metal oxide is as a Lewis acid,

Table 1 Comparison of catalyst performance in the conversion of glucose to lactic acid

Material name	Composition	Process parameter	Performance	Recyclability	References
Sn-beta zeolite	Sn incorporated beta zeolite	Temp.: 190 °C pressure: atmospheric [Glucose[a]]: 10 wt% Time: 2 h	Conv.: 98% Yield LA: 48%	Recyclable with slight loss	Dong et al.[12]
$ZnSO_4$	Zn sulfate salt	Temp.: 150–200 °C pressure: atmospheric [Glucose[a]]: 5–10 wt% Time: 2–4 h	Conv.: ND[b] Yield: 39%	Limited stability	Saulnier-Bellemare and patience[13]
Sn(II)/Al(III) bimetallic	Sn and Al mixed salts	Temp.: 200 °C Pressure: 10 bar N_2 [Glucose[a]]: 5 wt% Time: 3 h	Conv.: ND[b] Yield: 81%	Good recyclability	Saulnier-Bellemare and patience[13]
Erbium salts	Erbium salts	Temp: 150–180 °C Pressure: atm [Glucose[a]]: 2–5 wt% Time: 1–2 h	Conv.: ND[b] Yield: 81%	Poor recyclability	Saulnier-Bellemare and patience[13]
MgAl-LDH/carbon	Mg, Al LDH on carbon	Temp.: 150 °C Pressure: atm [Glucose[a]]: high Time: 2 h	Conv.: ND[b] Yield: 87% with NaOH	Moderate stability	Liu et al.[14]
Sn-beta-zeolite	Sn on beta zeolite ($SiO_2 : Al_2O_3 = 100$)	Temp.: 180 °C Pressure: 20 bar N_2 [Glucose[a]]: 10 wt% Time: 30 min	Conv.: ND[b] Yield: 76%	Stable after 5 cycles	Guo et al.[15]
Sn-beta zeolite	Template-free Sn-beta zeolite	Temp.: 200 °C Pressure: 40 bar He [Glucose[a]]: 10 wt% Time: 30 min	Conv.: ND[b] Yield: 67%	Recyclable	Sun et al.[16]
HR-Zr-BEA	Hierarchical Zr-BEA	Temp.: 180 °C Pressure: 3 bar N_2 [Glucose[a]]: 10 wt% Time: 3 h	Conv.: ND[b] Yield: 81%	Good recyclability	Cui et al.[17]
Zr-BEA	Zr incorporated beta zeolite	Temp.: 170 °C Pressure: 20 bar N_2 [Glucose[a]]: 10 wt% Time: 6 h	Conv.: more than 80% Yield: 81%	Recyclable	Dong et al.[12]

[a] [Glucose] concentration glucose. [b] ND not disclosed.

providing more binding sites for catalytic activity on the support surface. In addition to ZrO_2, other metal oxides such as SnO_2 have also been studied, where SnO_2 functions as an active component that facilitates the reaction by providing adsorption sites and promoting the desired chemical transformations. Both ZrO_2 and SnO_2 are typically associated with Lewis acid sites that promote the initial dehydration of glucose to intermediates such as levulinic acid, which can subsequently undergo hydrogenation to form lactic acid.

This paper reports on the preparation of Zr/Sn/Al-SBA-15 catalysts with varying loading of Zr and Sn in both mono-metallic and bimetallic catalysts for the conversion of glucose to D-lactic acid. The catalyst is synthesized from SBA-15 as a support, with an alumination step to modify the acidity properties of SBA-15, and a final impregnation with Zr and Sn metals to enhance the catalytic performance for the production of lactic acid. The choice of Sn is driven by its strong Lewis acidity, which is critical for catalyzing the glucose isomerization and retro-aldol reactions that lead to lactic acid formation. Zr is incorporated for its ability to provide both Lewis and Brønsted acid sites, as well as its robust thermal stability, which improves catalyst durability under reaction conditions. The bimetallic combination of Sn and Zr is expected to synergistically enhance catalytic activity by balancing Lewis and Brønsted acid sites, thereby improving selectivity and yield while minimizing side reactions. The high surface area of SBA-15 supports the dispersion of metal sites, facilitating accessibility and effective catalysis. The textural properties and catalytic performance will also be discussed.

Experimental

Materials

All the chemicals used for the preparation of the catalyst, reaction studies, and product analysis were obtained from Sigma-Aldrich Chemical and used as received without any purification. SBA-15 was employed as the support, with triblock co-polymer poly(ethylene glycol)-*block*-poly(propylene glycol)-*block*-poly(ethylene glycol), known as P123, used as the template, while tetraethyl orthosilicate (TEOS) was used as the silica source, and hydrochloric acid was used as the medium for the hydrolysis process. The SBA-15 support was subsequently modified by introducing aluminium, Al into the synthesis mixture using aluminium nitrate $Al(NO_3)_3 \cdot 9H_2O$ as Al source, in an alkaline medium containing aqueous tetra-methylammonium hydroxide, TMAOH. The Zr salt, zirconyl nitrate $(ZrO(NO_3)_2 \cdot 6H_2O)$, and the Sn salt, $(SnCl_2 \cdot 2H_2O)$ were then used to impregnate the support, with metal loading in the range of 5–10%. Distilled water was used as the solvent for all preparation steps.

Methods

Catalyst preparation

Synthesis of the SBA-15 support. SBA-15 was prepared by using the conventional procedure, as described by Mazinani *et al.*[19] A triblock copolymer P123 (8 g) was dissolved in distilled water (60 g) for 3 hours, then 240 g of 2 M HCl was added to the solution. The mixture was stirred at 40 °C for 2 h, then 18 g of the silica source, tetraethyl orthosilicate, was added dropwise while stirring, and the mixture was allowed to age for 24 h at 40 °C under an acidic environment. The mixture was placed in a stainless-steel autoclave for the hydrothermal process at 100 °C for 2 days under static conditions. The white powder was filtered and washed a few times using distilled water before drying in an oven at 100 °C overnight. The as-synthesized sample was calcined at 550 °C for 6 h.

Alumination of SBA-15. The alumination process was based on the method described by Gómez-Cazalilla *et al.*[20] and Vift-taria *et al.*[21] with an Si/Al ratio of 25 used in this experiment. An appropriate amount of 1.2 M of $Al(NO_3)_3 \cdot 9H_2O$ was mixed with 5.5 wt% TMAOH in a water solution. The mixed solution was stirred at 60 °C for 2 hours, then added to 1 g of pure silica SBA-15 under stirring for 1 h at 60 °C. The powder product was then washed and filtered using distilled water until the pH changed to neutral, then dried in an oven at 60 °C overnight. Lastly, the sample was calcined at 550 °C for 6 h at a rate of 5 °C min^{-1}. The sample was coding as Al-SBA-15.

Impregnated catalyst. Synthesized Al-SBA-15 was impregnated with 2, 6, and 10 wt% zirconium(II) nitrate hexa-hydrate $(Zr(NO_3)_2 \cdot 6H_2O)$ salt *via* the incipient wetness impregnation method. The synthesized Al-SBA-15 was fully dissolved in sufficient distilled water before Zr nitrate salt was added to the Al-SBA-15 aqueous solution. All the prepared catalysts were stirred for 3 h at room temperature and then dried at 100 °C for 12 h and calcined at 550 °C for 6 h. The same process was repeated to impregnate tin(II) chloride dihydrate salt $(SnCl_2 \cdot 2H_2O)$ with different ratio $x = 2$, 6 and 10 wt% of the synthesized xZr/Al-SBA-15 by using $y = 2$, 6 and 10 wt% tin(ll) chloride nitrate hexahydrate salts to synthesized bimetallic xZr/ySn/Al-SBA-15 with $x = 5$, 3, and 7 wt% and $y = 5$, 7 and 3 wt% ratio.

Catalyst characterization. Nitrogen adsorption–desorption analyses were performed with a Micromeritics ASAP 2020 (Norcross, GA, USA). Samples were pre-treated at 110 °C for 10 hours. The specific surface area of the catalyst was calculated by the multiple-point Brunauer–Emmet–Teller (BET) method in the relative pressure (P/P_o) range from 0.03 to 0.30. The Barrett–Joyner–Halenda (BJH) technique, which is based on thermo-dynamics, was employed to estimate the distributions of the pore size from the isotherm's desorption branch. At a relative pressure of 0.998, the adsorbed quantity of liquid nitrogen indicated the total volume of the pores by inspecting the adsorption branch of the N_2 isotherm.

Characterization of the crystallinity of the catalyst was performed using X-ray diffraction (XRD) (Bruker model X'pert3 Powder and Empyrean (PAN Analytical), Billerica, MA, USA). All measurements were made at low angle in the 2θ range 0.5–5° and wide angle in the range 10–80°, with a step size of 0.01° and 10 s step duration.

The acidic properties of the catalysts were measured using temperature-programmed desorption (TPD) (Thermo Scientific, TPDRO 1100) of ammonia (NH_3). Prior to the measurement, the catalyst was treated with helium (He) gas for 10 min at 20

mL min^{-1} to clean the surface of contaminants. The temperature was then increased to 500 °C at 10 °C min^{-1} and maintained for 120 min, then cooled to the adsorption temperature under a He atmosphere. Next, the NH$_3$ adsorption was performed at 100–150 °C with 5–10% NH$_3$/He for 60 minutes. The system was then cooled to 50 °C, pure He was switched back, and the system was purged for 60 minutes to remove physisorbed NH$_3$. The desorption step was then conducted in He flow at 20 mL min^{-1} with an initial temperature of 50 °C that ramped to 600 °C at 10 °C min^{-1} with an isothermal hold of 60 min at the final temperature.

Catalyst testing. Conversion of sugars was performed using an autoclave high-pressure reactor with a stainless-steel liner. An aqueous glucose solution with 10 wt% and 0.1 g of catalyst was added into the reactor vessel under continuous stirring. The autoclave was sealed by tightening all screws using an Allen key. The pressure at the gas regulator was adjusted to 5 bar. The atmosphere in the reactor was replaced three times with N$_2$ and then charged with 5 bar N$_2$. The reactor was heated to 200 °C for a reaction time of 3 h. After the reaction, the rector was left to cool to 25 °C and the chiller was turned on and set at 10 °C. The obtained liquid was collected in glass vials.

All catalysts were screened using the same screening parameters. The catalyst producing the highest amount of lactic acid was selected for pressure optimization, which was conducted in the range of 20 to 60 bar N$_2$. For this optimization, catalytic testing was performed at 210 °C for 3 h using 63 wt% of the catalyst with 3.16 g of glucose. Subsequently, the catalyst system that achieved the highest amount of lactic acid under the optimized pressure condition was submitted to temperature optimization in the range 150–230 °C. Under the same reaction conditions used for pressure optimization, the effect of temperature on lactic acid yield, as well as the formation of other by-products, was then measured.

The separation of the compounds was performed on an Agilent 1260 series HPLC equipped with an RI detector using an Aminex HPX-87H column (300 mm × 7.8 mm) with 5 mM H$_2$SO$_4$ as mobile phase with a flow rate of 0.4 mL min^{-1}, an injection volume of 0.1 μL, a column temperature of 55 °C, and a RID temperature set at 45 °C. The evaluation of the compounds was run for 25 min. The standard materials were obtained from Sigma-Aldrich Chemical (purity 99.9%). For qualitative analysis, the retention time was compared to that of standard materials, and the product and the glucose conversion and yield of the lactic acid were calculated from the equations below:

$$\text{Conversion}(\%) = \frac{\text{moles of glucose(in)} - \text{moles of glucose(out)}}{\text{moles of glucose(in)}} \times 100 \tag{1}$$

$$\text{Yield}(\%) = \frac{\text{moles of lactic acid}}{\text{moles of glucose}} \times 100 \tag{2}$$
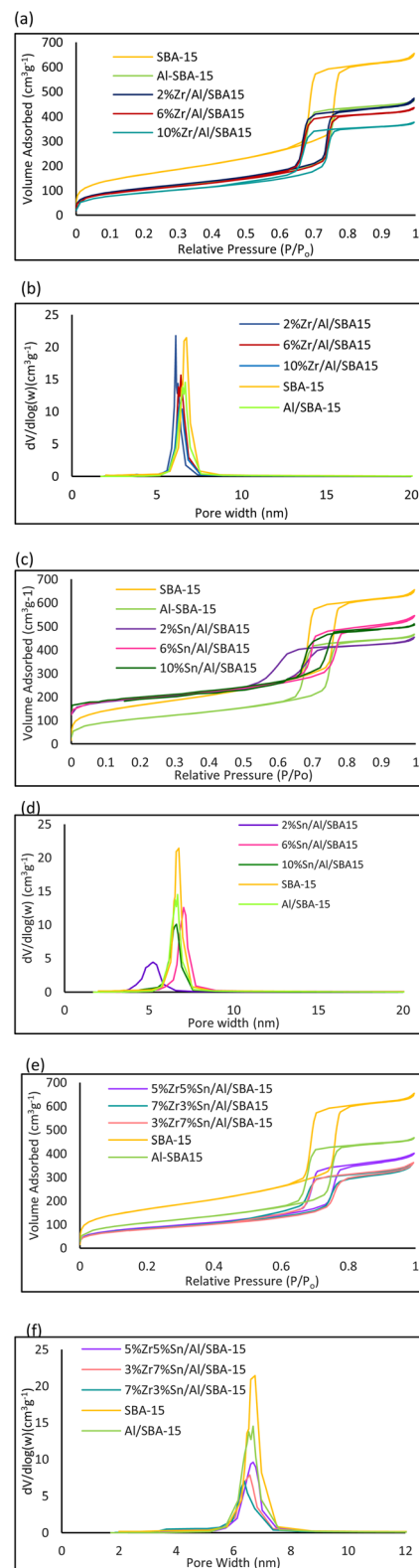

Fig. 1 Nitrogen adsorption–desorption isotherm of (a) Zr-impregnated Al-SBA-15 catalyst (c) Sn-impregnated Al-SBA-15 catalyst (e) bimetallic Zr/Sn-impregnated catalyst and BJH pore size distributions of (b) Zr-impregnated Al-SBA-15 catalyst (d) Sn-impregnated Al-SBA-15 catalyst (f) bimetallic Zr/Sn-impregnated catalyst.

Results and discussions

Catalyst characterization

The nitrogen adsorption–desorption isotherms and pore size distributions of all catalysts are shown in Fig. 1. According to the IUPAC classification, all samples have type IV isotherms with an H1-type hysteresis loop, indicating the formation of mesoporous materials with 1-D cylindrical channels.[22] The support, SBA-15, shows a sharp inflection at a relative pressure (P/P_o) between 0.6 and 0.8, which indicates a higher N_2 adsorption due to the multilayer adsorption in the formed mesopore. The sharp inflection of the SBA-15 isotherm reveals that the sample has a large pore size and pore volume at 6.93 nm and 0.85 cm³ g⁻¹, respectively, as tabulated in Table 1. However, after the alumination process, the hysteresis loop of Al-SBA-15 was slightly reduced compared to that of the original SBA-15 sample. Fig. 1(a) shows that aluminated SBA-15 has a low volume adsorbed, which suggests that the incorporation of Al affects the adsorption capacity due to partial pore filling of the support.[23] Tsai et al. described that the changes of the hysteresis loop depend on the metal loading dispersion, where higher metal loadings result in a reduction of the pore volume and surface area, which can significantly affect the shape of the hysteresis loop.[24] This feature can be observed in all the impregnated samples, with the hysteresis loop becoming smaller with lower volume adsorbed when the percent metal loading increases.

Generally, the isotherms for all impregnated samples are similar in shape when compared with the Al-SBA-15 isotherm. As the loading of Zr and Sn was increased, the inflection points of the step shifted to lower relative pressure (P/P_o) values, and the amounts of adsorption decreased, which indicates changes in the channel shape that are created from defects in the pore walls of the samples.

All Zr impregnated samples retain the same isotherm pattern but show a decrease in the volume of N_2, with a hysteresis loop observed at a low relative pressure (P/P_o) of 0.6–0.8. The higher the amount of impregnated Zr, the lower the volume adsorbed in the isotherm. This indicates that the lower the volume of N_2 adsorbed for the sample, the larger the pore size of the sample. This is due to some pores being blocked by the Zr metal. This finding is in agreement with that of Colmenares-Zerpa et al., who reported that the structural order of SBA-15 was greatly affected by loading Zr into its structure because of the reduction of the surface area and pore size with increasing pore volume of the sample.[25] As can be seen in Fig. 1(a), catalysts with higher Zr loading show decreased levels of adsorbed N_2 volume, which results in smaller hysteresis closing.

A slightly uncommon shape of the hysteresis loop for sample 2% Sn, in which the hysteresis occurred at a low relative pressure in the range 0.5–0.7, with a low amount of N_2 volume adsorbed, is seen in (Fig. 1(c)). The gradual increase in adsorption volume at lower pressure ranges suggested a broader distribution of pore sizes, as shown in the BJH pore size distribution graph in Fig. 1(d). This finding is consistent with research by Chen et al., which showed that a low percentage of Sn impregnation preserves the mesostructure, while higher loading disrupts the mesostructure of the support.[26] On the other hand, 6 and 10% impregnated Sn samples display similar hysteresis loop shapes, where hysteresis occurred at a high relative pressure (P/P_o) of 0.6–0.8. The introduction of higher Sn content into the support can change the surface chemistry of SBA-15, influencing the interaction between the adsorbate (nitrogen) and the adsorbent, contributing to the pressure shift on which the capillary condensation occurs.[27]

There is no significant difference in the hysteresis pattern for bimetallic catalyst samples of SBA-15 and Al-SBA-15. Fig. 1(e) shows that the hysteresis of the bimetallic samples has a low N_2 volume adsorbed, indicating that there is a decrease in the surface area and pore size of the bimetallic catalyst. All samples exhibit the characteristics of well-ordered mesoporous materials, as illustrated in the pore size distribution graph shown in Fig. 1(f). All the bimetallic samples show a sharp and narrow peak centred in the range 5–7 nm, but there is a slight decrease in pore volume as compared to that of the support SBA-15.

The pore sizes determined by the peak positions of the pore size distribution (PSD) profiles () are within 5–7 nm. The peak of

Table 2 Textural properties of Al–SBA-15 with different loadings of monometallic Zr/Al-SBA-15, Sn/Al-SBA-15 and different ratios of bimetallic Zr/Sn/Al-SBA-15

Catalyst	SBET (m² g⁻¹)[a]	d_p (nm)[b]	V_p (cm³ g⁻¹)[c]	Crystallite size (nm)
SBA-15	581	6.9	0.85	N.D.
Al-SBA15	380	7.3	0.69	N.D.
2%Zr/Al-SBA	386	6.9	0.63	N.D.
6%Zr/Al-SBA	367	7.5	0.65	N.D.
10%Zr/Al-SBA	321	7.4	0.56	N.D.
2%Sn/Al-SBA	330	6.4	0.53	3.8
6%Sn/Al-SBA	344	7.4	0.66	4.4
10%Sn/Al-SBA	340	7.6	0.61	16.9
5%Zr 5%Sn/Al-SBA	306	8.0	0.62	22.3
7%Zr 3%Sn/Al-SBA	296	7.3	0.56	13.1
3%Zr 7%Sn/Al-SBA	289	7.5	0.57	22.8

[a] Specific surface area. [b] Average pore diameter. [c] Pore volume N.D. = not detected.

the PSD profile broadened, and its height decreased after Zr and Sn were impregnated into Al-SBA-15. However, for the 2% Sn sample, the peak position shifted to the lower pore size range of 3–6 nm. This is consistent with the isotherm of the 2% Sn sample, where the hysteresis loop was observed at a lower relative pressure (P/P_o) with a smaller hysteresis than the other samples. This is due to Sn not being well-dispersed within the silica framework, which leads to the formation of large aggregates that block the pores of the support. For the bimetallic catalyst, the peak distribution becomes lower as compared to the monometallic catalyst, which suggests that Zr and Sn were incorporated as isolated metals and were highly dispersed without agglomeration on the support. It can be concluded that although a mix of Zr and Sn was impregnated, it did not lead to a change in the structure of the catalyst, except for the reduction in pore volume, as described in Table 2.

The specific surface area, pore volume, and pore size of the synthesized Zr- and Sn-impregnated Al-SBA-15 samples are listed in Table 2. The highest surface area was observed on SBA-15 as a support catalyst with 581 m^2 g^{-1}. The obtained results revealed that all the samples showed higher surface areas and porosity. However, after the introduction of metal oxide through alumination of Al and impregnation of Zr and Sn into Al-SBA-15, a decrease in the textural properties was observed. The Al-SBA-15 shows a significant reduction in surface area (to 380 m^2 g^{-1}) compared to SBA-15. The alumination process leads to a reduction in surface area and pore volume of the sample due to alkaline dissociation of the pore structure, which results in pore structure degradation, as noted by Kumaran et al.[28]

Impregnation of Zr and Sn shows varied properties depending on the amount of metal added. From the summarized textural properties in Table 2, both impregnated Zr and Sn show a decreasing pattern from 2% to 6% and gradually increase as Zr and Sn were introduced to 10%, which can be related to the hysteresis loop changes in 2% and 6% Sn and Zr loading. This is due to the interaction between metal and support for 2% to 6% of Zr and Sn, which can be explained through the pore-filling phenomenon.[29] Wang et al. also stated that metal impregnation from low to high loading can change the electronic environment and the distribution of active sites on the catalyst surface.[30] On the other hand, for the 10% Zr and Sn samples, the results indicate that the increases in textural properties are possibly due to improved metal dispersion or pore restructuring.[31] This result suggests a balance between pore-filling and structural stability, as referred to in a study by Al-Fatesh et al.[32] They also stated that impregnated metal was deposited much more prominently on the surface of the support than deposited as particles in the pores of the support. At the same total metal loading of 10%, the bimetallic textural properties do not lead to a significant change in the surface area, pore volume or pore size, as tabulated in Table 2. This indicates that Zr and Sn are well-dispersed and no agglomerated metal was present in the pores of the support.

The size of the Sn/Al-SBA-15 particles was calculated from the XRD line broadening of the peak at the (100) plane, using Scherrer's equation for all catalysts. The particle size can be detected from the Sn samples because Sn atoms tend to form

aggregation into crystalline SnO_2 nanoparticles even at low loading. In contrast, for SBA-15, Al-SBA-15 and Zr/Al-SBA-15 samples, their components remain amorphous and thus are not detectable in XRD. However, in the bimetallic catalyst, the crystallite size can be detected due to the domination of the Sn particles, despite its low loading in the catalyst. From Table 2, the bimetallic catalyst shows a higher crystallite size, with 22 nm crystallites for 5% Sn 5% Zr and 3% Zr 7% Sn, while monometallic 10% Sn gave 16 nm crystallite size.

Fig. 2 shows the low-angle XRD pattern, while Fig. 3 shows the wide-angle diffraction peaks of SBA-15, Al-SBA-15 and Al-
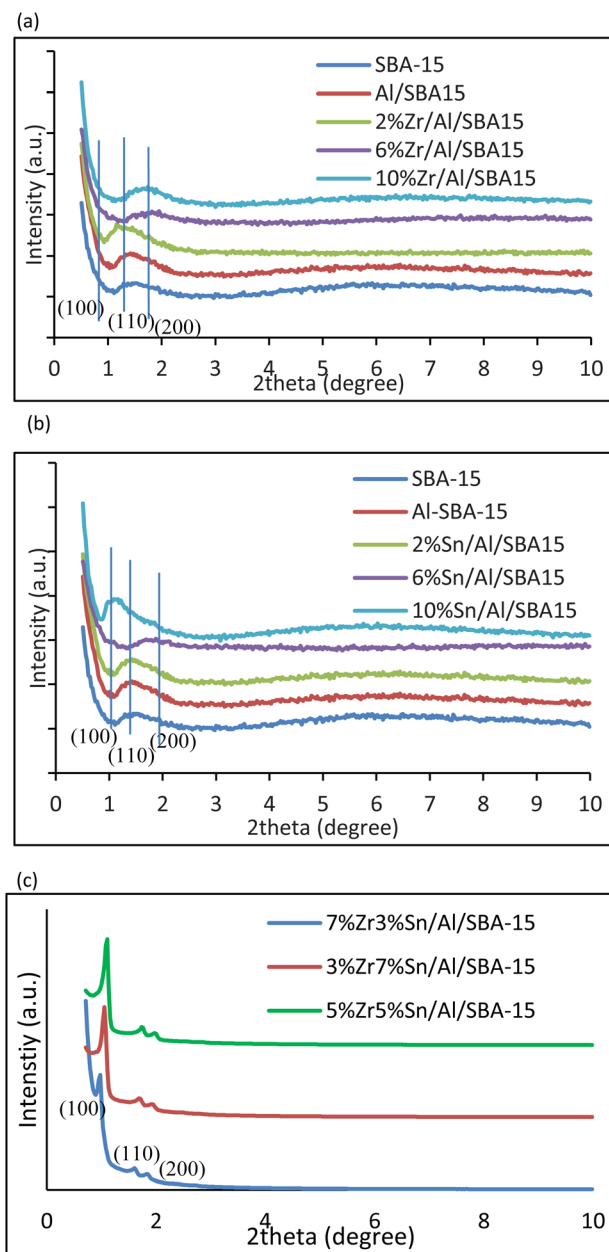

Fig. 2 X-ray diffraction analysis of the low-angle (a) Zr/Al-SBA-15 (b) Sn/Al-SBA-15 and (c) bimetallic catalyst.

SBA-15 with different metal loadings of Sn and Zr. The low-angle data of the SBA-15 support show three signature diffraction peaks at 2theta values of 0.92°, 1.55°, and 1.82°, which can be indexed as (100), (110), and (200) planes, respectively, as displayed in Fig. 2(a). These diffraction peaks correspond to the well-ordered two-dimensional hexagonal structure of SBA-15.[33] Although the intensities of the peaks show a decreasing pattern for Al-SBA-15 as one Al species was introduced into the support, the three planes of (100), (110), and (200) do not alter the lattice structure of SBA-15 as the Al atoms are incorporated mainly into the silica framework by substituting silicon atoms. The Al atoms grafted onto the internal pore surfaces introduce acidity to the catalyst without collapsing the structure of SBA-15 itself, as shown in Fig. 2(a) and (b).[34,35]

There were no diffraction peaks corresponding to Al_2O_3 on Al-SBA-15 materials, suggesting there was no formation of isolated Al_2O_3 clusters, and the Al^{3+} ions are well dispersed in the lattice without the formation of Al_2O_3 clusters.[36] The main diffraction peak for the (100) plane in the Al-SBA-15 sample was observed to shift to lower 2theta values, indicating an expansion of the lattice, which was attributed to the larger Al^{3+} radius compared to Si^{4+}. The expansion also implies less structural contraction and lengthened Al–O bonds than Si–O bonds.[37] Therefore, it can be concluded that the alumination process does not alter the ordered mesoporous phase. This conclusion was supported by the XRD low-angle pattern and the BET isotherm of Al-SBA-15, which shows a similar pattern to the parent SBA-15.

As Zr was added to the SBA-15 framework (Fig. 2(a)), the intensity of the (110) peak decreased while the (200) peak shifted to the right and appeared broader. The higher the Zr loading, the more the (110) and (200) planes shifted to higher 2theta, showing that the lattice had contracted. This result agrees with a report by Wang et al.[24] that suggested the incorporation of Al and Zr into SBA-15 led to no damage in the mesostructured SBA-15 framework. This observation is also consistent with the isotherms shown in Fig. 1, where the amount of absorbed N_2 decreases after the incorporation of Al and Zr into the pores of SBA-15.

Meanwhile, the Sn-impregnated sample shows no changes in the diffractogram of 2% Sn as compared to those of SBA-15 and Al-SBA-15. However, when 10% Sn was impregnated, the peaks for (110) and (200) shifted to lower 2-theta values, indicating that the lattice had expanded, thus altering the mesostructured order and textural properties of the samples. A similar behaviour is observed for the bimetallic catalysts (Fig. 2(c)) where the main diffraction peaks shift and a sharp (100) reflection appears, consistent with the well-defined Al-containing mesoporous structures without the formation of Al_2O_3 clusters.[36] The reflections from the (110) and (200) planes also become more intense than in the monometallic Sn/Al-SBA15 and Zr/Al-SBA-15 samples, indicating a higher degree of structural ordering.

From Fig. 3(a), the wide-angle XRD spectra of calcined samples showed only a broad hump for 2theta between 15° and 35°, indicating the amorphous structure of the walls. No crystalline phase of Zr was detected, suggesting that Zr is well-incorporated into the silica matrix and retains its amorphous properties. Zr also tends to be highly dispersed as small clusters within the SBA-15 framework or on the support surface, without modifying the parent SBA-15. For all the Zr-impregnated samples, the hump peak shifted to higher theta as compared to SBA-15, suggesting a contraction of the lattice, meaning that the d-spacing within the catalyst structure has decreased.[25]

The total acidity and acid strength profiles of the synthesized catalysts were characterized by NH_3-TPD. Following the previous study, the NH_3-TPD profile of the acidic catalyst is categorized into three regions, which are represented as weak (25–200 °C), moderate (200–400 °C), and strong acids (at
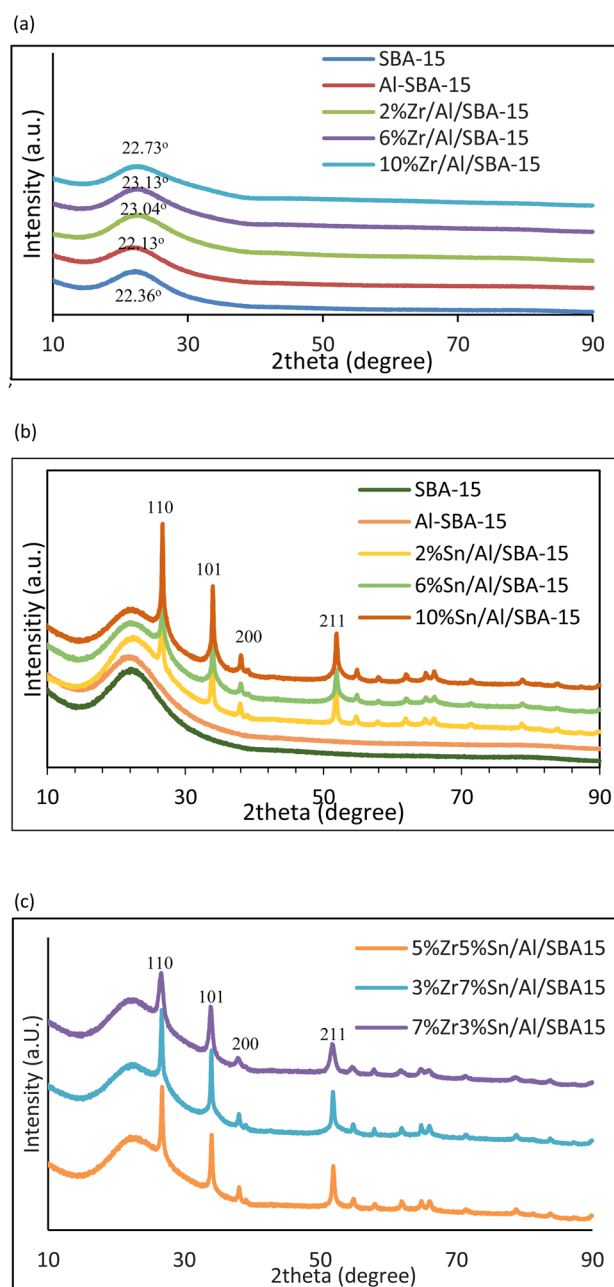

Fig. 3 X-ray diffraction analysis of the wide-angle (a) Zr/Al–SBA-15 (b) Sn/Al-SBA-15 and (c) bimetallic catalyst.

temperatures above 400 °C).[38] Fig. 4 shows the NH_3-TPD profiles of all the synthesized samples. The results reveal that the parent SBA-15 samples do not exhibit acidity properties, showing only

Fig. 4 NH_3-TPD profiles of synthesized (a) SBA-15, alumination catalyst, and (b–d) Zr/Sn impregnate samples.

a very small low-temperature response that can be attributed to weakly acidic surface silanol (Si–OH) groups rather than catalytically relevant acid sites. This is in agreement with previous reports on siliceous SBA-15 supports that show that the surface of the SBA-15 is dominated by silanol hydroxyl (Si–OH) groups, which limit the capacity to donate H^+ ions and are considered almost inactive in typical acid-catalysed transformations.[39] Catalytic activity is only observed after introducing stronger Brønsted or Lewis acid centres through post-synthetic modifications.

Upon alumination, the Al-SBA-15 catalyst exhibits a distinct desorption peak at approximately 105 °C, corresponding to weak acid sites with an ammonia uptake of 102.34 $\mu molg^{-1}$, as tabulated in Table 3. This behaviour is consistent with the study by Jeon et al.,[40] who showed that incorporation of aluminium into the SBA-15 framework significantly increases the total acidity, with Al-containing materials displaying much higher acid site densities than the parent silica due to Al species located on or near the silica surface being readily accessible to reactant molecules during catalytic reactions.

The effect of alumination on the parent support and the impact of subsequent Zr incorporation on the acidity of Al-SBA-15 were then examined. All the Zr-modified samples show two distinct peak desorptions in the NH_3-TPD profiles (Fig. 4(b)). A low-temperature peak at 99 °C is assigned to weak acid sites, with the corresponding acidity increasing in the order 6% Zr (1.43 $\mu mol\ g^{-1}$), 2% Zr (2.22 $\mu mol\ g^{-1}$) and 10% Zr (4.38 $\mu mol\ g^{-1}$). In addition, all the Zr-containing samples exhibit a broad peak centered around 280 °C, with a tail extending to about 400 °C, indicative of medium-to-strong acid sites. The position of the peak at this high-temperature feature is nearly independent of Zr loading, while the amount of desorbed NH_3 attributed to medium sites rises from 0.56 $\mu mol\ g^{-1}$ (6% Zr) and 0.68 $\mu mol\ g^{-1}$ (2% Zr) to 5.8 $\mu mol\ g^{-1}$ for the 10% Zr catalyst. This behavior suggests that increasing the Zr content mainly increases the number of medium/strong acid sites without significantly altering their intrinsic acid strength.

The evolution of the acidity pattern with Zr loading can be explained by the distribution of ZrO_2 species on the Al-SBA-15
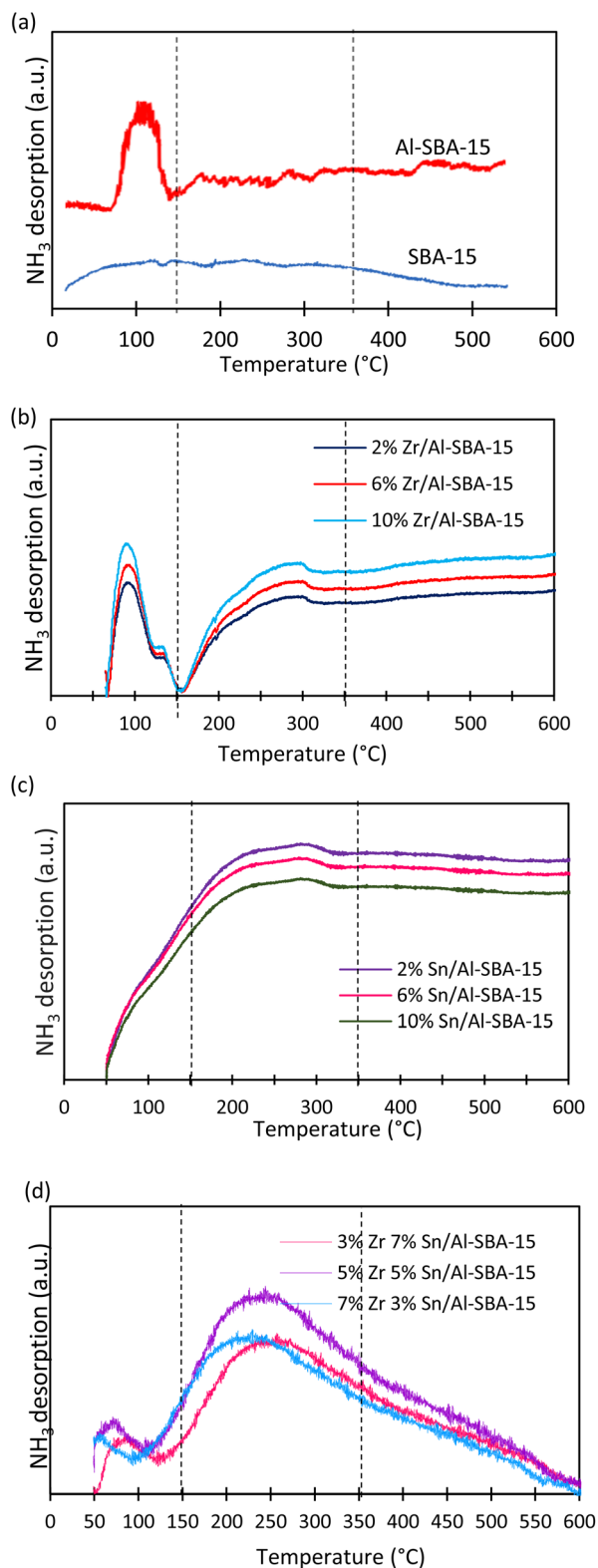
Table 3 Acidic properties of the synthesized catalysts

Catalyst	Weak ($\mu mol\ g^{-1}$)	Medium ($\mu mol\ g^{-1}$)	Strong ($\mu mol\ g^{-1}$)
SBA-15	ND[a]	ND[a]	ND[a]
Al-SBA-15	102.34	ND[a]	ND[a]
2% Zr/Al-SBA-15	2.23	0.68	ND[a]
6% Zr/Al-SBA-15	1.44	0.57	ND[a]
10% Zr/Al-SBA-15	4.38	5.80	ND[a]
2% Sn/Al-SBA-15	ND[a]	23.39	ND[a]
6% Sn/Al-SBA-15	ND[a]	0.73	ND[a]
10% Sn/Al-SBA-15	ND[a]	19.93	ND[a]
5% Zr 5% Sn/Al-SBA-15	1.66	ND[a]	6.59
3% Zr 7% Sn/Al-SBA-15	1.54	ND[a]	22.74
7% Zr 3% Sn/Al-SBA-15	1.30	ND[a]	1.78

[a] ND = Not detected.

Paper

surface. At low (2% Zr) and intermediate (6% Zr) Zr contents, most Zr is expected to form isolated Zr–O–Si/Zr–O–Al species, which introduce only a limited number of Lewis acid sites; this is manifested as relatively small amounts of weak and medium sites in the NH$_3$-TPD.[41] As the Zr loading increases to 10% Zr, these species become more abundant and distorted, which increases the number and strength of accessible Lewis acid centres without shifting the desorption peaks to much higher temperatures, so the intrinsic acidity remains similar while the site population grows. This observation is similar to those of da Silva *et al.* and Calzada *et al.*, who reported that NH$_3$-TPD shows that the total amount of acid sites and the fraction of medium sites rise with Zr content, while the peak positions remain nearly unchanged, and the acidity is attributed to framework or surface Zr–O–Si moieties rather than bulk ZrO$_2$.[41,42]

The NH$_3$-TPD profiles of the Sn-modified catalysts are shown in Fig. 4(c), while the amounts of desorbed NH$_3$ are tabulated in Table 3. The Sn introduction fundamentally changed the acidity of Al-SBA-15 toward predominantly medium-strength Lewis sites, in contrast to the weak acidity of Al-SBA-15 and the weak-to-medium distribution observed for the Zr-loaded samples. None of the Sn/Al-SBA-15 materials exhibits a distinct low-temperature peak, and the deconvolution confirms the absence of weak sites, while medium acidity is substantial for 2% Sn (23.39 µmol g^{-1}) and 10% Sn (19.93 µmol g^{-1}) but almost suppressed for 6% Sn (0.73 µmol g^{-1}). This behaviour suggests that at low and high Sn loadings, the Sn species are well dispersed as isolated or small oligomeric Sn–O–Si/Sn–O–Al units that act as accessible Lewis acid centres, whereas at 6% Sn a fraction of the Sn likely aggregates or resides in less accessible environments, leading to a drastic reduction in titratable sites without a major change in desorption temperature.

Such a dominance of medium Lewis acidity on Sn-modified mesoporous silicas is consistent with previous reports on Sn-SBA-15 and related Sn-containing catalysts, where NH$_3$-TPD and probe reactions identify Sn^{4+} centres in tetrahedral or highly distorted octahedral coordination as the origin of medium-strength Lewis sites suitable for sugar isomerization and retro-aldol chemistry. At 2 and 10 wt% Sn, a large fraction of Sn is likely present as isolated or small Sn–O–Si/Sn–O–Al species on the pore surface, which behave as accessible, medium-strength Lewis sites and give high NH$_3$ uptake in the medium region. This finding is the same as that reported for active Sn-SBA-15 and Sn-beta catalysts in glucose and fructose transformations.[43,44] At 6 wt% Sn, part of the Sn probably aggregates into less dispersed SnO$_x$ domains and occupies less accessible positions inside the pores, meaning fewer Sn centres are available to interact with NH$_3$. For this reason, the desorption temperature stays in the medium range, but the quantified acidity drops sharply.

In addition, the NH$_3$-TPD profiles for bimetallic Zr–Sn/Al-SBA-15 catalysts display a low-temperature shoulder between about 80 and 150 °C, together with a broad, asymmetric peak extending from roughly 150 to 500 °C, whose intensity depends on the Zr/Sn ratio (Fig. 4(d)). Deconvolution of these curves shows that all three samples contain only a small number of weak sites (1.30–1.66 µmol g^{-1}), whereas strong acidity

dominates and varies markedly with composition, rising from 1.78 µmol g^{-1} for 7% Zr–3% Sn to 6.59 µmol g^{-1} for 5% Zr–5% Sn and reaching 22.74 µmol g^{-1} for 3% Zr–7% Sn. The similar position of the main high-temperature feature in the three traces, combined with the large differences in integrated strong-acid populations, suggests that the Zr/Sn ratio mainly controls the number of highly acidic sites rather than their intrinsic strength, with Sn-rich formulations favouring the formation of a larger density of strong Lewis/Brønsted centres.

The acidity pattern observed for the bimetallic Zr–Sn/Al-SBA-15 catalysts can be rationalised by cooperative effects between zirconium and tin species anchored on the aluminosilicate framework. Co-incorporation of Zr and Sn favours the formation of mixed Zr–O–Sn and highly distorted M–O–Si/M–O–Al (M = Zr, Sn) environments, which are known to generate stronger acid centres than those produced by either metal alone. In Sn-rich samples, a larger fraction of Sn is likely involved in such heterometallic or defect-rich sites rather than in isolated medium-strength Lewis centres, leading to the substantial increase in the strong acid population quantified for the 3% Zr–7% Sn material. At the same time, the nearly unchanged position of the main high-temperature desorption feature across the series implies that the fundamental nature of these strong sites is similar, and that changing the Zr/Sn ratio primarily alters their concentration.

Catalyst testing

All the synthesized catalysts were evaluated for catalytic performance in producing lactic acid from glucose as a feedstock, as illustrated in Fig. 5. Screening tests were performed at a temperature of 200 °C under inert conditions with nitrogen gas at 5 bar for 3 h using a high-pressure batch reactor with a fixed mass of feedstocks (6.32 g), and catalyzed by 0.1 g of catalyst. The yields of lactic acid and glucose conversion were calculated using a linear equation generated from a calibration curve constructed by measuring standard D-lactic acid and glucose, respectively, at five different concentrations.

Among all the monometallic catalysts, the 2% Sn sample achieved the highest yield of lactic acid of 4.1%, while the
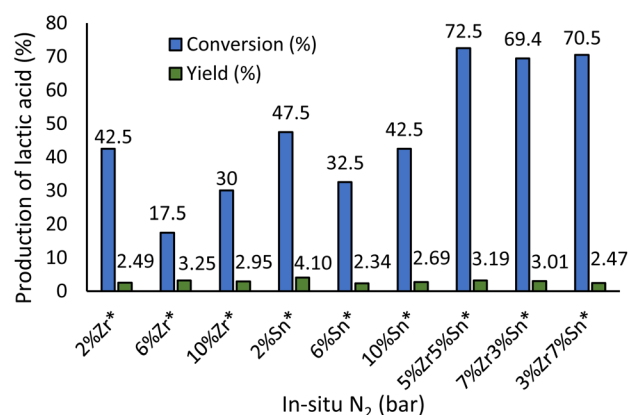

Fig. 5 Catalyst screening of the synthesized catalyst for the conversion of glucose to lactic acid at 200 °C for 3 h at 5 bar. *Al-SBA-15

conversion of glucose was 47.5%, followed by 6% Zr, with a lactic acid yield of 3.25% and 17.5% glucose conversion. The results show that Sn is more effective than Zr for achieving lactic acid yield under these screening conditions. Sn and Zr provide strong Lewis acid sites for the isomerization of glucose to fructose and retro-aldol cleavage of fructose steps. However, the results show that the Sn catalyst has a higher number of Lewis sites than the Zr catalyst. As reported by Deng *et al.*, catalysts with a combination of Sn(II) and Al(III) gave a lactic acid yield of 81% from glucose under high-temperature conditions,[34] while the Zr catalyst could only achieve a lactic acid yield of around 21% under stable hydrothermal conditions[13] owing to the moderate Lewis acidity.

As described earlier, isomerization and retrol-aldol cleavage need a Lewis acid for conversion activity. The bimetallic catalysts gave better yields and conversions, with 3.19% yield and 72.5% conversion of glucose for the 5% Zr 5% Sn catalyst, followed by 3.01% yield of lactic acid with 72.5% glucose conversion recorded for the 7% Zr 3% Sn catalyst. The combination of Zr and Sn somehow decreases the catalytic activity due to solvent adsorption on the active site of the catalyst, coke formation and metal leaching. This reduced activity of the bimetallic catalyst is still under review by our group. In this study, the bimetallic catalyst produced more solid residues and side products than the monometallic catalysts, which contributed to their lower apparent catalytic activity.

The activity and selectivity of lactic acid formation from the glucose in the catalytic conversion strongly depend on the properties of the catalyst, which cover acidity, basicity, metals, particle size, and support. These catalyst properties will improve the conversion activity when coupled with suitable operating reaction conditions. However, the screening process of catalytic conversion was done with a high concentration of feedstock (6.32 g glucose) and a relatively low amount of catalyst (0.1 g), indicating an insufficient catalyst loading to effectively catalyze the reaction. During the conversion, Lewis acid sites coordinate with the carbonyl oxygen of glucose, facilitating its isomerization to fructose. Subsequently, these Lewis acid sites will assist the fructose to undergo direct retro-aldol cleavage, producing C3 intermediates dihydroxyacetone and glyceraldehyde, which serve as precursors to lactic acid. The Lewis acid sites play a crucial role in stabilizing the reaction intermediates and lowering the activation energy required for this cleavage step.[45]

Effect of reaction pressure

The study was extended by examining the effect of various nitrogen pressures (20, 30, 40, 50 and 60 bar) in the presence of 63 wt% of 2% Sn/Al-SBA15 catalyst at 210 °C for 3 hours of reaction with 3.16 g of glucose as feedstock. Due to the possibility of glucose forming other products, the study on different nitrogen pressures was performed to establish the optimal pressure conditions for maximum lactic acid yield, before it starts to degrade or produce side products. A slight increase in lactic acid yield was observed when the pressure was increased from 20 to 50 bar, reaching a maximum yield of 25.2% at 50 bar,

and the yield trend started to slightly decline at 60 bar, with 24.9% yield of lactic acid. The conversion showed a consistent trend with insignificant changes in value as the pressure was elevated to 60 bar of nitrogen. The decline in performance at elevated pressure suggests that the catalytic reaction did not proceed to a high degree under high-pressure conditions. The higher lactic acid yield attained at higher pressure might be because fructose in the intermediate reaction step generates dihydroxyacetone or glyceraldehyde through retro-aldol, which requires a higher energy to initiate the cleavage of the C–C bond before it reaches a desirable condition for the formation of other products, which also explains the higher conversion of glucose.[46] It has been reported that lactic acid could be converted to formic acid and acetic acid under high-pressure conditions with water as the medium.[47] However, the slightly declining trend observed at 60 bar nitrogen pressure might be because the decomposition rate of lactic acid is higher than the production rate at this pressure.[36] This behaviour is consistent with the observations of Sun *et al.*,[16] who reported that increasing the pressure enhanced lactic acid yields up to 40 bar, but further increases in pressure led to a decreases in pressure in yield because of intensified side-reaction pathways.

Effect of reaction temperature

The effect of reaction temperature was further studied. A range of temperatures from 150 to 230 °C was applied under 50 bar nitrogen pressure with glucose and catalyst weights of 3.16 g and 2.0 g, respectively. Fig. 6 shows that, with 2% Sn/Al/SBA-15 catalyst, higher temperatures give higher yields of lactic acid. At a temperature range of 190 to 230 °C, higher lactic acid yields were achieved, but no further increment was observed in this series. Meanwhile, at a temperature range of 150 to 170 °C, 14% lactic acid yield was obtained, and it can be concluded that lactic acid will increase at higher temperatures under suitable reaction conditions.

Limited research had confirmed that lactic acid yield was influenced by reaction temperatures in the range of 170 to 210 °C. Sun *et al.*[48] found that a maximum lactic acid yield of around 57.9% was achieved when the temperature was increased to 200 °C for 30 min reaction under 40 bar helium using a Sn-Beta catalyst, while Zahari *et al.*[46] found that elevating the reaction temperature from 120 to 190 °C increased the lactic acid
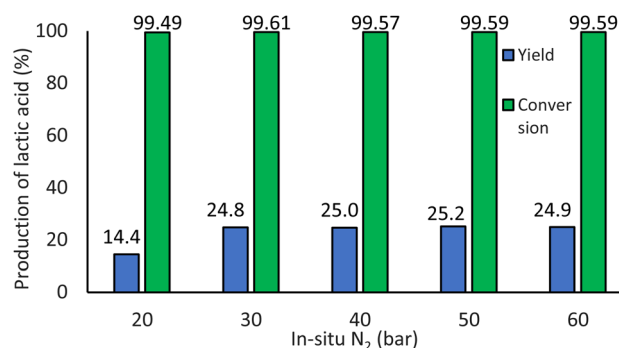

Fig. 6 Effect of reaction pressure using 2%Sn/Al/SBA-15 as the catalyst for the conversion of glucose to lactic acid at 210 °C for 3 h.

product yield, with the best temperature above 160 °C, using hydrothermal conversion and different metal ions as a catalyst.

At lower temperatures, Sun et al.[48] reported that the formation of fructose was increased to 47.6%, together with other by-products such as xylitol, levulinic acid and 5-HMF. This finding agrees with ours. At a temperature of 150 °C, other by-products, especially fructose, were observed, indicating that the rate of isomerization of the intermediates is greater than the rate of fructose conversion to lactic acid.[49]

At 150 °C, the conversion of glucose was reduced to 83.84%, while at 170 °C to 230 °C a high glucose conversion of 98 to 99% was observed. The high conversion is due to the increase in molecular kinetic energy, which accelerates the glucose diffusion and interaction with active sites on the catalyst surface. High temperatures will enhance the activation and catalytic efficiency of Lewis acid sites at Sn and Brønsted acid sites at Al in the retro-aldol reaction steps for breaking the C–C bond in fructose to produce the smaller C_3 compounds glyceraldehyde and dihydroxyacetone. It also found that higher temperatures promote the formation of other by-products such as levulinic acid, formic acid, acetic acid and humin (Table 4).

To detect the by-products, standards for all the compounds were analyzed using HPLC, following the same method applied for lactic acid determination. The chromatograms of each by-product were compared with those of the sample, and yields were quantified using calibration curves prepared from five different concentrations of each compound.

The effect of temperature revealed that levulinic acid and formic acid were the major by-products formed during the conversion. The highest levulinic acid yield (29.33%) occurred at 170 °C, while formic acid reached its maximum yield (28.29%) at 190 °C. Referring to Fig. 7, lactic acid yields at 170 °C and 190 °C were relatively low, at only 14% and 21%, respectively, but began to increase significantly at 210 °C. At this temperature, levels of levulinic and formic acid remained comparatively high.

This pattern suggests that, at lower temperatures (170–190 °C), competing pathways such as retro-aldol cleavage and dehydration dominate, leading to the formation of levulinic and formic acids rather than lactic acid. As the temperature increases to 210 °C, the catalytic activity of the Lewis acid sites becomes more effective for converting the C3 intermediates (dihydroxyacetone and glyceraldehyde) into lactic acid,
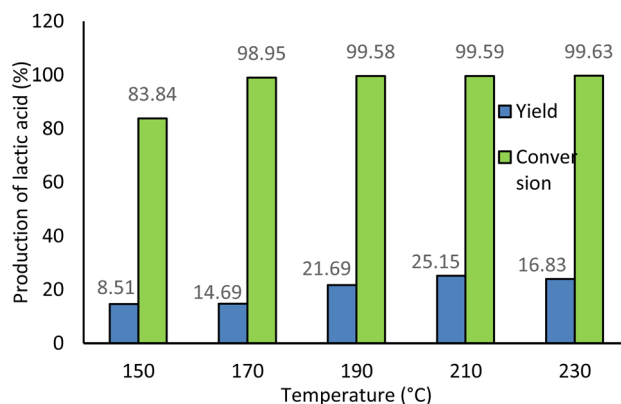

Fig. 7 Effect of reaction temperature using 2% Sn/Al/SBA-15 as the catalyst for the conversion of glucose to lactic acid at 50 bar N_2 for 3 h.

resulting in higher lactic acid yield. Under certain conditions, especially at high temperatures or strong acidity, the C3 intermediates can undergo further fragmentation, producing formic and levulinic acid.[50] However, the persistence of levulinic and formic acids at 210 °C indicates that side reactions still occur, limiting the maximum selectivity toward lactic acid.

Conclusions

Lactic acid was successfully produced from glucose using a high-pressure batch reactor under 5 bar of N_2 inert conditions at a high temperature of 200 °C for 3 h, catalysed by monometallic and bimetallic catalysts. The monometallic catalyst 2% Sn/Al-SBA-15 shows a higher activity, with a lactic acid yield of 4% during the screening process. The study confirms that careful tuning of catalyst composition and reaction parameters is crucial for maximizing lactic acid production from biomass-derived glucose, offering a sustainable alternative to traditional fermentation methods.

Author contributions

Conceptualization, A. R.; methodology, F. M. J.; software, F. M. J.; validation, A. R., L. J. W and N. B.; formal analysis, F. M. J.; investigation, F. M. J.; resources, A. R., L. J. W and N. B.; data curation, F. M. J.; writing – original draft preparation, F. M. J.; writing – review and editing, A. R.; visualization, A. R., L. J. W and N. B; supervision, A. R., L. J. W and N. B; project administration, A. R.; and funding acquisition, A. R., L. J. W and N. B. All authors have read and agreed to the published version of the manuscript.

Conflicts of interest

There are no conflicts to declare.

Data availability

All data are contained within the article.

Table 4 Effect of temperature on by-product yields of glucose conversion using 2% Sn/Al-SBA-15 catalyst

2% Sn/Al-SBA-15 Temperature (°C)	Levulinic acid Yield (%)	Formic acid Yield (%)	Acetic acid Yield (%)	Fructose Yield (%)
150	3.55	ND	ND	35.6
170	29.33	25.83	0.2	1.79
190	13.72	28.29	0.35	1.28
210	22.81	16.98	0.82	2.27
230	19.58	14.00	0.84	1.64

Acknowledgements

Notes and references

1 A. A. Marianou, C. M. Michailof, A. Pineda, E. F. Iliopoulou, K. S. Triantafyllidis and A. A. Lappas, *Appl. Catal., A*, 2018, **555**, 75–87.

2 D. Esposito and M. Antonietti, *ChemSusChem*, 2013, **6**, 989–992.

3 F. A. Castillo Martinez, E. M. Balciunas, J. M. Salgado, J. M. Domínguez González, A. Converti and R. P. D. S. Oliveira, *Trends Food Sci. Technol.*, 2013, **30**, 70–83.

4 M. H. Yaacob, MSc thesis, Universiti Sains Malaysia, 2018.

5 M. Shakeri, Z. K. Shal and P. Van Der Voort, *Materials*, 2021, **14**, 5082.

6 B. Dragoi, E. Dumitriu, C. Guimon and A. Auroux, *Microporous Mesoporous Mater.*, 2009, **121**, 7–17.

7 Z. Li, P. Wu, J. Pang, X. Li, S. Zhai and M. Zheng, *Catalysts*, 2012, **13**, 545.

8 S. N. M. Saleh and A. Z. Abdullah, *Chem. Rev.*, 2021, **12**, 2565–2578.

9 H. Qin, Yu-H. Zhang, Z. Wang and G. Yang, *Catalysts*, 2022, **12**, 719.

10 A. O. Ojo and O. de Smidt, *Processes*, 2023, **11**, 688.

11 M. Alexandri, R. Schneider, K. Mehlmann and J. Venus, *Food Technol. Biotechnol.*, 2019, **57**, 293–304.

12 W. Dong, Z. Shen, B. Peng, M. Gu, X. Zhou, B. Xiang and Y. Zhang, *Sci. Rep.*, 2016, **6**, 26713.

13 T. Saulnier-Bellemare and G. S. Patience, *ACS Omega*, 2024, **9**(22), 23121–23137.

14 X. Liu, Z. Liu, Q. Zhang, H. Wu and R. Wang, *J. Chem.*, 2020, **2020**, 1–7.

15 F. Guo, Y. Wang, Z. Jiang, Y. Tu, R. Li, X. Zhang, A. Tang, Y. Liang, L. Yan, H. Luo, S. Li and L. Kong, *Molecules*, 2025, **30**, 1457.

16 Y. Sun, L. Shi., H. Wang., G. Miao., L. Kong., S. Li and Y. Sun, *Sustain. Energy Fuels*, 2019, **3**(5), 1163–1171.

17 Y. Cui, J. Li, Z. Liu, H. Yu, D. Ding and J. Wang, *Microporous Mesoporous Mater.*, 2023, **360**, 112737.

18 P. Wattanapaphawong, O. Sato, K. Sato, N. Mimura, P. Reubroycharoen and A. Yamaguchi, *Catalysts*, 2017, **7**, 221.

19 B. Mazinani, A. Beitollahi, A. K. Masrom, S. Ibrahim and F. Jamil, *AIP Conf. Proc.*, 2012, **1502**, 272–279.

20 M. Gómez-Cazalilla, J. M. Mérida-Robles, A. Gurbani, E. Rodríguez-Castellón and A. Jiménez-López, *J. Solid State Chem.*, 2007, **180**, 1130–1140.

21 M. Vifttaria, N. Nurhayati and S. Anita, *J. Phys., Conf. Ser.*, 2019, **1351**, 012040.

22 S. T. Phạm, M. B. Nguyen, G. H. Le, T. Pham, T. T. T. Quan, T. D. Nguyen and T. L. Son, *J. Chem.*, 2019, **55**, 369–453.

23 M. S. M. de Oliveira, L. Biesekia, A. E. Valentim de Alencar, T. P. Braga and S. B. Castellã Pergher, *Mater. Res.*, 2019, **22**(3), e20180657.

24 J. H. Tsai, Y. T. Chen and C. H. Tsai, *Nanomaterials*, 2023, **13**, 1106.

25 J. Colmenares-Zerpa, J. Gajardo, A. Peixoto, D. Silva, J. Silva, F. Gispert-Guirado, J. Llorca, E. Urquieta-Gonzalez, J. Santos and R. Chimentão, *J. Solid State Chem.*, 2022, **312**, 123296.

26 S. Chen, H. Tsai, W. Chuang, J. Lee, C. Tang, C. Lin and S. Cheng, *J. Phys. Chem. C*, 2009, **113**(34), 15226–15238.

27 M. Füredi, C. V. Manzano, A. Marton, B. Fodor, A. Alvarez-Fernandez and S. Guldin, *J. Phys. Chem. Lett.*, 2024, **15**(5), 1420–1427.

28 G. M. Kumaran, S. Garg, K. Soni, M. Kumar, J. Gupta, L. Sharma, K. R. Rao and G. M. Dhar, *Microporous Mesoporous Mater.*, 2008, **114**(1–3), 103–109.

29 S. K. Bhatia and H. K. Shethna, *Langmuir*, 1994, **10**(9), 3230–3243.

30 Y. Wang, W. Deng, B. Wang, Q. Zhang, X. Wan, Z. Tang, Y. Wang, C. Zhu, Z. Cao, G. Wang and H. Wan, *Nat. Commun.*, 2013, **4**, 2141.

31 Ó. De La Iglesia, M. Sarango, M. Munárriz, M. Malankowska, A. Navajas, L. M. Gandía, J. Coronas and C. Téllez, *ACS Sustain. Chem. Eng.*, 2022, **10**(9), 2868–2880.

32 A. S. Al-Fatesh, R. Kumar, S. O. Kasim, A. A. Ibrahim, A. H. Fakeeha, A. E. Abasaeed, H. Atia, U. Armbruster, C. Kreyenschulte, H. Lund, S. Bartling, Y. A. Mohammed, Y. A. Albaqmaa, M. S. Lanre, M. L. Chaudhary, F. Almubaddel and B. Chowdhury, *Catal. Today*, 2019, **348**, 236–242.

33 M. Adrover E., M. Pedernera, M. Bonne, B. Lebeau, V. Bucalá and L. Gallo, *Saudi Pharm. J.*, 2019, **28**(1), 15–24.

34 Y. Deng, J. Zhou, G. Li, H. Liu, X. Gao, Y. Yue, H. Li, F. Xie and H. Liu, *Inorg. Chem.*, 2022, **61**(30), 11820–11829.

35 H. Kao, C. Ting and S. Chao, *J. Mol. Catal. Chem.*, 2005, **235**(1–2), 200–208.

36 O. F. Aldosari, M. S. Alhumaimess, M. A. Betiha, E. A. Ahmed, L. M. Alhaidari, A. Altwala and H. M. A. Hassan, *Catalysts*, 2023, **13**(11), 1395.

37 Y. Liu, Y. Cao, N. Yi, W. Feng, W. Dai, S. Yan, H. He and K. Fan, *J. Catal.*, 2004, **224**(2), 417–428.

38 F. Arena, R. Dario and A. Parmaliana, *Appl. Catal., A*, 1998, **170**, 127–137P.

39 S. Krishnan, U. Samidurai, V. G. Balashanmugam, H. S. Kim and P. Aghalayam, *Sep. Purif. Technol.*, 2023, **320**.

40 M. J. Jeon, J. K. Jeon, Y. K. Park, S. H. Park and S. H. Lee, *Appl. Catal., B*, 2013, **129**, 429–436.

41 L. A. Calzada, D. Pérez-Estrada, M. A. Macías-Montero, J. J. González and M. Montes, *ACS Omega*, 2023, **8**, 44247–44261.

42 J. Colmenares-Zerpa, J. Gajardo, A. F. Peixoto, D. S. A. Silva, J. A. Silva, F. Gispert-Guirado, J. Llorca, E. A. Urquieta-Gonzalez, J. B. O. Santos and R. J. Chimentão, *J. Solid State Chem.*, 2022, **312**, 232–247.

43 Y. Zhu, X. Xu, W. Zhao, M. Yue and K. Song, *Front. Chem.*, 2021, **9**, 817417.

44 L. A. Calzada, D. Pérez-Estrada, M. A. Macías-Montero, J. J. González and M. Montes, *ACS Omega*, 2023, **8**, 44247–44261.

45 T. Fang, M. Liu, Z. Li, L. Xiong, D. Zhang, K. Meng, X. Qu, G. Zhang, X. Jin and C. Yang, *Chin. J. Chem. Eng.*, 2022, **53**, 381–401.

46 S. M. S. N. S. Zahari, N. A. Zulastry and H. H. Azman, *J. Phys.: Conf. Ser.*, 2020, **1551**, 012014.

47 J. Shen, C. Chen, C. Huang, Y. Shi and H. Xu, *ACS Omega*, 2022, **7**, 17885–17897.

48 Y. Sun, L. Shi., H. Wang., G. Miao., L. Kong., S. Li and Y. Sun, *Sustain. Energy Fuels*, 2019, **3**(5), 1163–1171.

49 L. Li, F. Shen, R. L. Smith Jr and X. Qi, *Green Chem.*, 2017, **19**, 76–81.

50 X. Zhang, *Photocatal.: Res. Potential*, 2025, **2**, 10009.